



Mesoporous SBA-15 promoted by 3d-transition and noble metals for catalytic combustion of acetonitrile

Runduo Zhang, Dongjun Shi, Ning Liu, Yu Cao, Biaohua Chen*

State Key Laboratory of Chemical Resource Engineering, Beijing University of Chemical Technology, Beijing 100029, PR China



ARTICLE INFO

Article history:

Received 7 October 2012

Received in revised form 13 February 2013

Accepted 12 March 2013

Available online 25 March 2013

Keywords:

Mesoporous

Cu/SBA-15

Acetonitrile

Catalytic combustion

Mechanism

ABSTRACT

A series of M/SBA-15 [M = 3d transition metals (Cu, Co, Fe, V, Mn) and noble metals (Pd, Ag, Pt)] catalysts was prepared via an impregnation method, and further characterized by XRD, N₂ physical adsorption, TEM, H₂-TPR and XPS as well as activity test for CH₃CN + O₂ reaction. Ordered mesoporous structure of SBA-15 was well maintained even after impregnating the various metallic components. The CH₃CN conversion of the investigated catalysts follows a trend of Pt > Pd > Cu > Co > Fe > V > Ag > Mn > SBA-15. Apart from the target product of N₂, harmful byproducts (NO, NO₂, N₂O, NH₃ and CO) were also observed during the catalytic combustion. The corresponding activities and selectivities were verified to be associative with both redox properties and chemical natures of the loaded metals. Among the prepared M/SBA-15 samples, Cu/SBA-15 exhibited a nearly complete CH₃CN conversion associated with a N₂ selectivity around 80% at T > 350 °C, being regarded as a promising material for the catalytic removal of nitrile gases. Moreover, the activities of the Cu supported on different substrates (SBA-15, Al₂O₃, and SiO₂) were comparatively investigated and with the results indicating that SBA-15 is the proper candidate as a support for copper. Furthermore, the CH₃CN catalytic combustion mechanism was studied by DRIFTS. Four kinds of mechanisms were proposed to be essentially dependent on the physicochemical nature of the loaded metals and their supports, as well as the reaction temperature, with a priority formation of N₂ or NH₃ or N₂O or NO, respectively.

© 2013 Elsevier B.V. All rights reserved.

1. Introduction

Nitrile gases such as acetonitrile (CH₃CN), acrylonitrile (C₂H₃CN), and hydrocyanic acid (HCN) commonly classified as very toxic nitrogen-containing volatile organic compounds (VOCs) can lead to seriously environmental problems because of their hazardous properties. These pollutants in the gas phase are able to affect human beings and even be lethal at ppm levels in air [1–4]. Their effective removals by either incineration or catalytic combustion thus become necessary in order to control the air quality of our surviving environments. The traditional combustion with air has been studied earlier, as reviewed by Dagaout et al. [1]. However, the extremely high temperature for combustion readily leading to the NO_x (NO, NO₂) formation and the requirement of additional fuel consumption made this approach rather unattractive. Conversely, the relatively lower operation temperature for catalytic combustion associated with a less NO_x formation made this technology especially suitable for gaseous nitrile elimination. Effort for searching the effective catalytic materials never ceased.

Noble metal catalysts were found to be undesirable for HCN oxidation because of the poor activity of Rh/TiO₂ at low temperature [5,6] and the prior conversion to NO_x for Pd/TiO₂ and Pt/TiO₂ [7–10]. The high cost is another reason to limit their practical applications. Among the transition-metals, zeolite- or titania-supported copper catalysts were reported to show the ideal performances for nitrile combustion [2,11,12]. For example, 2.3 wt% Cu/ZSM-5 with an ion-exchange ratio of 57% and a specific surface area of 290 m² g⁻¹ was prepared by Nanba et al. [3,11] and thereafter used for acrylonitrile combustion. Isolated Cu²⁺ ions were deemed as the active sites and square planar type Cu²⁺ ions show particularly high activity. In addition, Solymosi and Kiss proposed a combustion mechanism involving the oxidation of adsorbed CN⁻ species via isocyanide species to CO₂ on Cu (1 1 1) [13]. Conversely, on Fe/ZSM-5 catalysts, the formation of both HNCO and CO₂ is invisible, which indicates that HCN catalytic removal takes place primarily via reactant dissociation and further hydrolysis to NH₃ and CO [12]. Obviously, the mechanism for selectively catalytic combustion of gaseous nitrile is still far away from well established.

Aside from HCN and C₂H₃CN, much attention was recently paid to the catalytic elimination of the harmful acetonitrile (CH₃CN), coming from the tail gas of industrial acrylonitrile (C₂H₃CN) plant in significant amounts, because of its toxicity. Acetonitrile can be readily decomposed into the highly toxic HCN in the body once it

* Corresponding author. Tel.: +86 10 64412054; fax: +86 10 64419619.

E-mail address: chenbh@mail.buct.edu.cn (B. Chen).

directly contacted with the human being; therefore, it belongs to one kind of toxic gases. Unfortunately, scarce data could be literaturely found for the CH_3CN abatement.

Mesoporous SBA-15 zeolite constitutes one kind of the excellent catalyst support due to its superhigh surface area, ordered pore arrangement, adjustable pore sizes from 3 to 30 nm, and high hydrothermal and thermal stability [14,15]. In our previous work [16], we primarily investigated the catalytic performances of Cu/, Co/, Cr/, Mn/SBA-15 for CH_3CN combustion, wherein the long term activity evaluations were also conducted. The results revealed that Cu/SBA-15 not only possessed the highest CH_3CN conversion and N_2 selectivity, but also exhibited a high stability during the long term evaluations. Nevertheless, the related mechanisms were still ambiguous and need to be finely studied. The catalyst screening should also be conducted on a larger scale. As a continuation, a wide range of transition metals modified SBA-15 samples (M/SBA-15) [M=3d transition metals (Cu, Co, Fe, V, Mn) and noble metals (Pd, Ag, Pt)] was prepared and characterized by X-ray diffraction (XRD), N_2 adsorption, transmission electron microscopy (TEM), temperature-programmed reduction by hydrogen (H_2 -TPR), X-ray photoelectron spectroscopy (XPS) as well as the activity tests for selectively catalytic combustion of CH_3CN in the presence of O_2 . Emphasis will be placed on both promoting the low-temperature activity and enhancing the N_2 selectivity via a modification of SBA-15 by transition or noble metals. In the light of above analyses, the relationship between the physicochemical properties of prepared catalysts and their depollution performances was clarified. Additionally, the influence of the different supports (SBA-15, Al_2O_3 , SiO_2) on CH_3CN catalytic combustion was also investigated. Moreover, an attempt to propose the related combustion mechanism has been done based on the diffuse reflectance infrared Fourier transform spectra (DRIFTS) studies.

2. Experimental method

For the sake of brevity, the experimental methods including catalyst preparation, characterization for physicochemical property, characterization for mechanism study, and activity test were simplified in the section with the specific descriptions being detailedly described in Supplementary material (SM) of Experimental section.

2.1. Catalyst preparation

The mesoporous SBA-15 was synthesized by a template method as detailedly described in Supplementary material of Experimental method section or in our previous paper [15]. The samples of metal modified SBA-15 (M/SBA-15, M= Cu, Co, Fe, V, Mn, Pd, Ag, Pt) as well as Cu supported on the other different carriers (Al_2O_3 , SiO_2) were prepared by means of an impregnation method with a total metal loading of 2 wt%.

2.2. Characterization for physicochemical property

X-ray diffraction (XRD) patterns were acquired on a Rigaku D/max 2500VB2 diffractometer operating at 40 kV and 200 mA with $\text{Cu K}\alpha$ irradiation and nickel filter ($\lambda=0.15406\text{ nm}$). The chemical compositions of the catalyst samples were determined by AXIOS advanced wavelength dispersive X-ray fluorescence spectrometer (XRF) (PANalytical). Specific surface areas, pore-size distributions, pore total volumes and sorption isotherms of the solids were measured via N_2 adsorption/desorption at -196°C using an automated gas sorption system (Sorptomatic 1990, Thermo Electron). The morphology of powder was studied by high resolution transmission electron microscopy (HRTEM) with a magnification of 500,000 \times using a JEOL J-3010 instrument operated at 200 kV. X-ray photoelectron spectroscopy (XPS) was conducted on a Thermo Fisher

ESCALAB 250 system with $\text{Al K}\alpha$ radiation under ultrahigh vacuum (UHV), calibrated internally by carbon deposit C(1s) having a binding energy (BE) at 284.6 eV. Temperature-programmed reduction by hydrogen (H_2 -TPR) and temperature-programmed oxidation by O_2 (O_2 -TPO) were conducted at the same equipment system. The detailed experimental strategies were listed in Supplementary material of Experimental methods.

2.3. Characterization for mechanism study

Diffuse reflectance infrared Fourier transform spectra (DRIFTS) were obtained using a Bruker TENSOR 27 system equipped with a MCT detector. The catalyst ($\sim 0.1\text{ g}$) was ground in an agate mortar and subsequently placed into the diffuse reflectance cell (Harrick) fitted with KBr windows and a heating cartridge that allowed samples to be heated up to the desired temperature ($<400^\circ\text{C}$). All spectra were collected with a resolution of 4 cm^{-1} and an accumulation of 100 scans.

2.4. Activity test

Activity measurement was performed in a quartz fixed-bed reactor (3 cm i.d.) under an atmosphere of 1 vol% CH_3CN and 5 vol% O_2 , balanced by He with a space velocity of approximate 20,000 h^{-1} . The effluent gases (CH_3CN , NH_3 , N_2O , NO, NO_2 , CO and CO_2) were monitored using an infrared gas analyzer (Nicolet Nexus 670) equipped with a 2.4 m long-path gas cell and TQ analysis software, while N_2 and O_2 were monitored using a gas chromatograph (GC, HP 5890) equipped with TCD and separated by columns of 5 A molecular sieve and TDX-01.

3. Results and discussion

3.1. Structural characterizations

Fig. 1a displays the small-angle XRD patterns of the prepared SBA-15 samples. Three diffraction peaks at $2\theta=0.94$, 1.6, and 1.8° respectively indexed as (1 0 0), (1 1 0), and (2 0 0) $h\ k\ l$ reflections of $P6mm$ symmetry are clearly discernable from the corresponding profile for the parent SBA-15, verifying the formation of typical SBA-15 silica with well-ordered and hexagonally structured mesoporous channels according to the earlier study [8]. As for the M/SBA-15 samples, their XRD patterns agree well with that of the parent SBA-15, except for the slight alterations in the intensities and positions of the prominent diffraction peak (1 0 0), indicating some deteriorations of the ordered pore structures occurred after the metals loading. As inferred from **Table 1**, the d -spacing values of the (1 0 0) plane for the SBA-15 samples are almost constant accompanying with the introduction of metals, suggesting these metal species are finely distributed in the mesoporous channel in the forms of either cations or metal oxides without obviously modifying the structural parameters of mesoporous SBA-15.

The wide-angle XRD patterns of (Cu, Co, Fe, V, Mn)/SBA-15 in **Fig. 1b** display no metal-oxide diffraction peaks for the (Cu, Co, Fe, V, Mn)/SBA-15, revealing that the metals mainly existed as the cationic species over the SBA-15 substrate. However, the related metal oxides cannot be totally ruled out as the contents are probably under the XRD detection limit. The broad peak at 2θ of about 22° is ascribed to the amorphous silica.

Fig. 1c displays the wide-angle XRD patterns of (Pd, Ag, Pt)/SBA-15. For Pd/SBA-15 the diffraction peaks of 33.7° , 41.9° , and 54.5° can be respectively indexed to (1 0 1), (1 1 0), and (1 1 2) lattice planes of PdO according to the JCPDS card of 43-1024. The diffraction pattern of Ag/SBA-15 displays three peaks of 32.3° , 37.8° and 54.5° , being attributed to the (1 1 1), (2 0 0), and (2 2 0) reflections of Ag_2O (JCPDS card of 76-1393), respectively. As for Pt/SBA-15 two

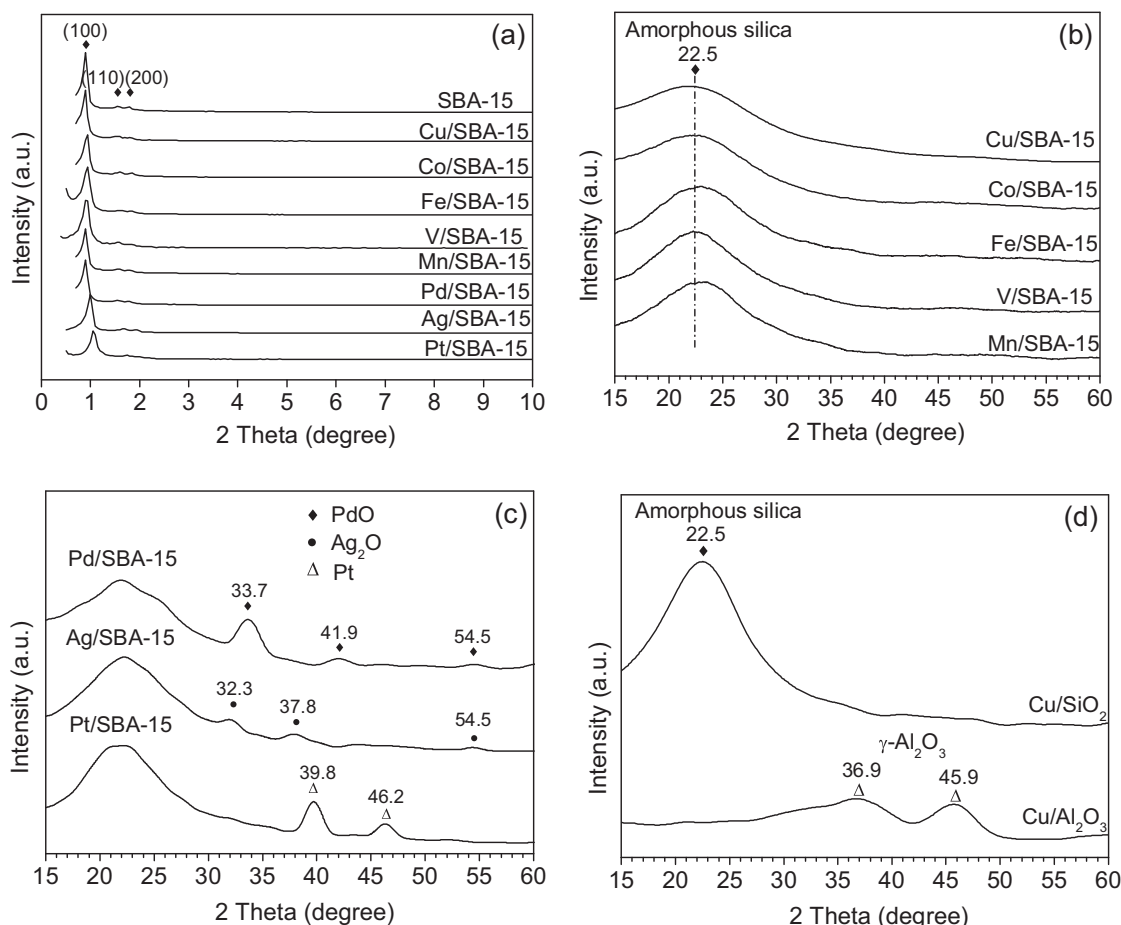


Fig. 1. (a) Small-angle XRD patterns of (Cu, Co, Fe, V, Mn, Pd, Ag, Pt)/SBA-15; (b) wide-angle XRD patterns of (Cu, Co, Fe, V, Mn)/SBA-15; (c) wide-angle XRD patterns of (Pd, Ag, Pt)/SBA-15; (d) wide-angle XRD patterns of Cu/SiO₂ and Cu/Al₂O₃.

diffraction peaks of 39.8° and 46.2° are clearly observed, which are individually corresponding to the (1 0 0) and (2 0 0) planes of the cubic Pt metal particles (JCPDS card of 04-0802). It should be noted that the segregation of Pt in zeolite is a common phenomenon involving migration of Pt from the channels to the external surface forming Pt nanoparticles [17]. The particle sizes of metal oxides on (Pd, Ag)/SBA-15 as well as Pt clusters on Pt/SBA-15 were further calculated by the Scherrer equation based on the most intense reflections, as listed in Table 1. Fig. 1d profiles the wide-angle XRD patterns of the Cu/SiO₂ and Cu/Al₂O₃. No obvious CuO or Cu⁰ peaks (JCPDS card of 80-1268, 2θ of 35.5 and 38.7°) can be observed, again

implying that the formed copper species are finely dispersed on the SiO₂ and Al₂O₃ substrates.

The textural properties of the samples were further studied by N₂ adsorption (not shown). The typical IV isotherm and H1-type hysteresis loop are observed for the synthesized SBA-15 samples, being consistent with the characteristic feature of mesoporous materials having one-dimensional cylindrical channels [14]. According to the report of Kaliaguine et al. [18], the initial increase in adsorption capacity at relatively lower pressures ($P/P_0 < 0.1$) is assigned to monolayer adsorption on the micropores' surface as well as monolayer and initial multilayer adsorption in the

Table 1
Chemical compositions and textural properties of M-BEA (M = Cu, Co, Fe, V, Mn, Pd, Ag, Pt), Cu/Al₂O₃ and Cu/SiO₂.

| Sample | Specific surface area (m ² g ⁻¹) | Crystallite size (nm) ^a | Pore volume (cm ³ g ⁻¹) | | | Mean pore diameter (nm) | d ₁₀₀ (nm) | Cell parameter a ₀ (nm) | Wall thickness (nm) |
|-----------------------------------|---|------------------------------------|--|----------|-------|-------------------------|-----------------------|------------------------------------|---------------------|
| | | | Micropore | Mesopore | Total | | | | |
| SBA-15 | 672 | – | 0.12 | 0.97 | 1.09 | 6.5 | 9.8 | 11.3 | 4.8 |
| Cu/SBA-15 | 575 | – | 0.09 | 0.80 | 0.89 | 6.2 | 9.8 | 11.3 | 5.1 |
| Co/SBA-15 | 588 | – | 0.11 | 0.74 | 0.85 | 5.8 | 9.8 | 11.3 | 5.5 |
| Fe/SBA-15 | 614 | – | 0.11 | 0.74 | 0.85 | 5.5 | 9.3 | 10.7 | 5.2 |
| V/SBA-15 | 503 | – | 0.08 | 0.66 | 0.74 | 5.9 | 9.5 | 11.0 | 5.1 |
| Mn/SBA-15 | 579 | – | 0.09 | 0.75 | 0.84 | 5.8 | 9.8 | 11.3 | 5.5 |
| Pd/SBA-15 | 632 | 25.4 | 0.13 | 0.82 | 0.95 | 6.0 | 9.8 | 11.3 | 5.3 |
| Ag/SBA-15 | 460 | 8.9 | 0.00 | 0.64 | 0.64 | 5.6 | 9.3 | 10.7 | 5.1 |
| Pt/SBA-15 | 402 | 7.2 | 0.00 | 0.63 | 0.63 | 6.3 | 9.8 | 11.3 | 5.0 |
| Cu/Al ₂ O ₃ | 312 | – | 0.00 | 0.70 | 0.7 | 9.0 | – | – | – |
| Cu/SiO ₂ | 324 | – | 0.00 | 0.86 | 0.86 | 10.6 | – | – | – |

^a Calculated by Scherrer equation based on wide-angle XRD peaks of the loaded metallic particles.

mesopores' intrawall. Thereafter, the upward deviation at higher P/P_0 of 0.4–0.8 is believed to be associated with the progressive filling of mesopores in the main channels by a process of capillary condensation. As shown in Table 1, the surface area of SBA-15 support is reduced to some degree after the active metals doping, suggesting the metal nanoparticles were incorporated into the mesoporous channels and possibly deposited on the mouth of SBA-15 channels. Additionally, it is also found that a drop in the pore size and a rise in the wall thickness occur simultaneously with the addition of active components. These findings further evidence that some metal species are confined inside the SBA-15 channels.

For the purpose of clarifying the pore architecture of the SBA-15 samples, the TEM measurements were conducted showing the image of (100) and (110) planes, wherein the orderly 2D hexagonal arrays with uniform pore sizes and parallel-arranged channels were clearly observed in Fig. 2A. The long-range mesoporous-ordering characteristic reflects a good-quality of this SBA-15 structured material without being remarkably disturbed by the introduction of the metals, which supports the above low-angle XRD and N_2 sorption results. The pore diameters as well as the wall thicknesses of the samples estimated by TEM are found to be consistent with those calculated by BJH method with the values respectively being of ~6 and ~5 nm. Moreover, the spherical nanoparticles (dark dot zone) are observed for Pd/, Ag/, and Pt/SBA-15, which can be attributed to the related metal oxides of Pd/, Ag/SBA-15 and the Pt nanoclusters of Pt/SBA-15, as verified by the wide-angle XRD. The particle size distributions derived from TEM images are shown in Fig. 2B, revealing these PdO_x nanoparticles of Pd/SBA-15 with the diameters being much larger than the pore diameters (~6 nm) mainly deposited outside the SBA-15 channels. Nevertheless, the AgO_x or Pt clusters with their domain sizes comparable to those of SBA-15 pores were confined inside the mesoporous channels. Additionally, it can also be found that the particle sizes derived from TEM are consistent with those calculated from XRD (see Table 1). However, for the other 3d transition metal ions (TMI) modified SBA-15 samples no metal clusters can be observed, suggesting that these TMI species are mainly distributed over the mesopore intra-surface.

3.2. Redox properties

In this section the reducibilities of the prepared samples are investigated by the H_2 -TPR, as shown in Fig. 3a–c. The quantitative calculations of the corresponding H_2 consumptions were summarized in Table 2.

As shown in Fig. 3a, the high stability of SBA-15 structure is confirmed with no reduction peak being observed in the investigated temperature region (50–700 °C). As for Cu/SBA-15 two reduction peaks are visible. The relationship between the intensity of the first peak and that of the second one allows us to assign that the first peak at 228 °C is mainly attributed to the reduction of divalent copper cations, and the other one (288 °C) is due to the successive reduction of ($Cu^+ \rightarrow Cu^0$) [19]. As listed in Table 2 for Cu/SBA-15, the H/Cu ratio of the first peak (0.94) is slightly higher than that of the latter one (0.92), which is speculated that the reduction of tiny amount of CuO to Cu^0 is involved in the first peak of 228 °C. The profile of Co/SBA-15 exhibits three reduction patterns, wherein the former two peaks (322, 457 °C) are respectively assigned to the reductions of $Co_3O_4 \rightarrow CoO$ and $CoO \rightarrow Co^0$ [20]; the latter one at 670 °C is ascribed to the reduction of Co^{2+} cations [21], which cannot be easily reduced by H_2 . Two reduction peaks centered at 419 and 626 °C are discerned from the H_2 -TPR of Fe-BEA, which respectively represent the reductions of cationic $Fe^{3+} \rightarrow Fe^{2+}$ with the H/Fe ratio of 0.90 (<1.0) and iron oxides [22]. The further reduction of Fe^{2+} to Fe^0 commonly occurs at $T > 800$ °C.

The H_2 -TPR profiles of V/ and Mn/SBA-15 display only one reduction peak. According to the literature reports [23,24], the peak at 645 °C for V/SBA-15 is correlated with the reduction of highly dispersed monomeric or low oligomeric VO_x ; and the reduction peak at 470 °C for Mn/SBA-15 corresponds to the reduction of MnO_x . Therefore, it can be found that: (I) highly dispersed metallic cations exist as the main species on Cu/, Co/, and Fe/SBA-15, whereas metal oxides are the predominant species on V/, and Mn/SBA-15; (II) the redox abilities, according to the temperature of the first reduction peak and the corresponding H_2 consumption, rank in an order of $Cu^+ > Co^+ > Fe^+ > Mn^+$; (III) although the H_2 -TPR verified the existence of the metal oxides over (Cu, Co, Fe, V, Mn)/SBA-15, especially for Mn/ and V/SBA-15, XRD displayed no diffraction peaks for these oxides, indicating that these metal oxides are well dispersed on the intra-surface of SBA-15 or too tiny to be XRD visible, as also evidenced by the TEM.

Fig. 3b depicts the H_2 -TPR of the noble-metal modified SBA-15 with Cu/SBA-15 as the reference. TPR plots of Ag/ and Pt/SBA-15 were enlarged twice for a better comparison. The profile of Pd/SBA-15 displays only one intense peak (118 °C), being related to the reduction of PdO [25]. The H/Pt ratio is calculated to be 1.78 comparable to the theoretical value for $PdO \rightarrow Pd^0$ reduction with a $H/Pd = 2.0$. As for Ag/SBA-15 three reduction peaks (193, 310, and 510 °C) were clearly observed. The former two peaks are respectively assigned to the reduction of the Ag_2O species deposited outside and inside the SBA-15 pores, while the latter one is associated with the reduction of the Ag^+ ions [26]. Three reduction patterns, one main peak (157 °C) associated with its shoulder (330 °C), as well as another small peak centered at 630 °C are found for Pt/SBA-15. According to the literature reports [27,28], (I) the H_2 -TPR reduction peak of PtO_x nanoparticles commonly occurred at $T < 25$ °C for those dispersed on the surface of zeolite and at the temperature around 80 °C for those deposited inside the zeolite channels; (II) divalent Pt^{2+} cations, strongly coordinated with the zeolite framework, exhibited a reduction peak approximately at 150 °C; (III) Pt^{4+} species of $Pt-(O-Si\equiv)_y^{2-y}$ can be readily formed through a coordination of platinum ions with the silanol (SiOH) groups of the SBA-15 framework during Pt/SBA-15 preparation and displaying the H_2 -TPR reduction peaks at 300–400 °C; (IV) H_2 reduction of the bulk PtO particles took place at the temperature range of 400–800 °C. Accordingly, the main peak at 157 °C can be related to the reduction of Pt^{2+} cations; the small shoulder at 330 °C is related to the reduction of small amount of Pt^{4+} species [$Pt-(O-Si\equiv)_y^{2-y}$]; and the small flat peak (630 °C) can be assigned to the reduction of bulk PtO particles, indicating that trace amount of PtO former on Pt/SBA-15. It should also be noted that H_2 consumption determined by the corresponding TPR peaks of Pt/SBA-15 is quite limited representing a H/Pt of 0.32. These findings reflect that only small part of platinum is in an oxidative form, whereas large amount of platinum exist in the form of Pt^0 nanoparticles being inert for H_2 reduction, as also evidenced by the XRD, and TEM. Therefore, metal oxides are found to be the main species on Pd/ and Ag/SBA-15, while metallic Pt clusters are of majority on the surface of Pt/SBA-15. Additionally, compared with Cu/SBA-15 the redox abilities of the noble-metal modified SBA-15 decreases in a sequence of $Pd \approx Pt > Cu > Ag/SBA-15$.

H_2 -TPR of Cu supported on Al_2O_3 and SiO_2 are shown in Fig. 3c (with Cu/SBA-15 as a reference), in which the reduction peaks at 290 °C (with a small shoulder at 326 °C) for Cu/ Al_2O_3 and 333 °C for Cu/ SiO_2 correspond to the reduction of CuO [29,30]. The values of the total H/Cu for Cu/ Al_2O_3 and Cu/ SiO_2 are respectively calculated to be 1.6 and 1.92, which are close to the theoretical value for the reduction of $CuO \rightarrow Cu^0$ (H/Cu = 2.0). Generally speaking, the redox abilities follow the trend of Cu/SBA-15 > Cu/ Al_2O_3 > Cu/ SiO_2 . It can be revealed that SBA-15 possessing higher specific surface area and special topology facilitates the dispersion of the loaded

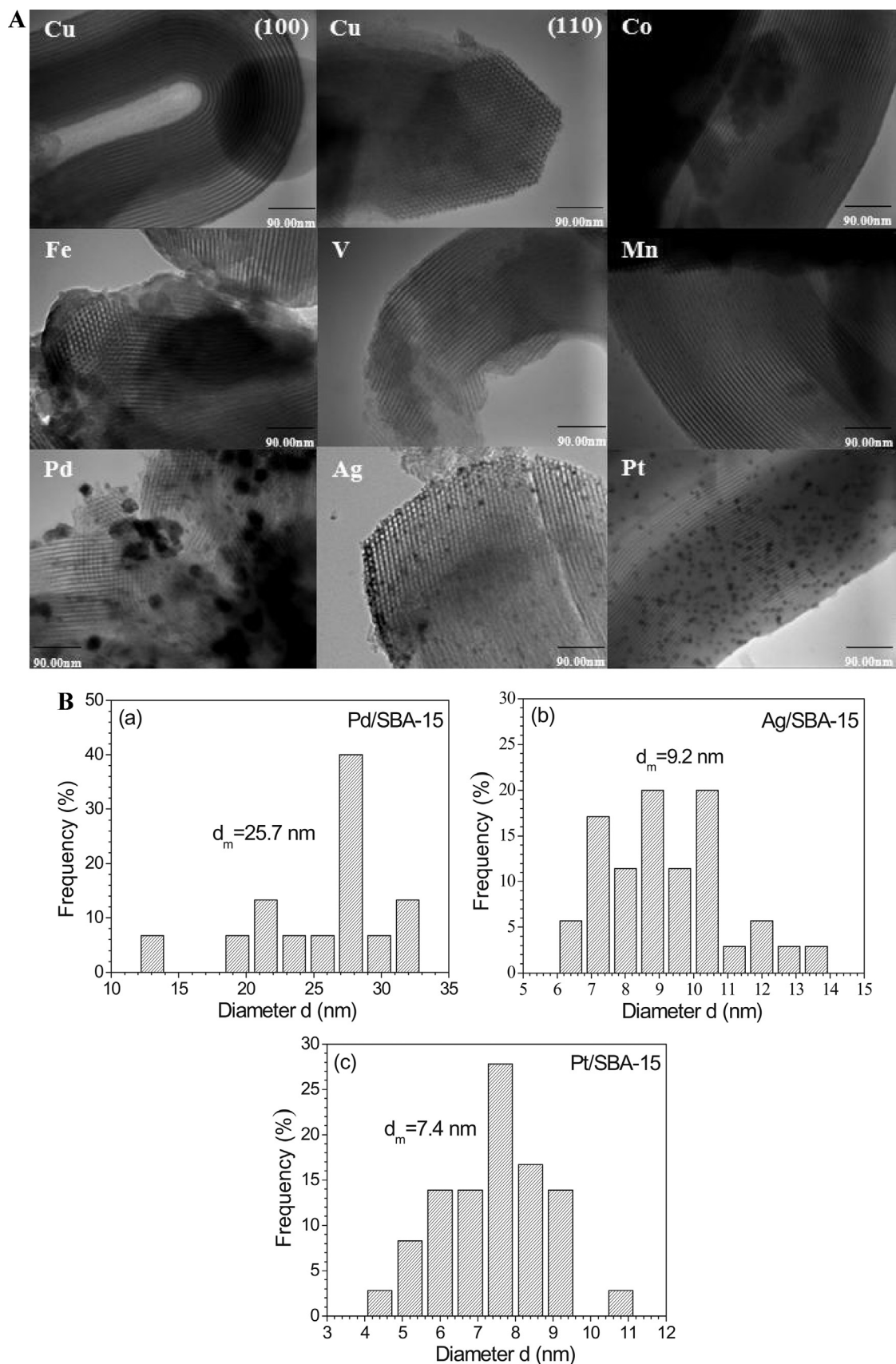


Fig. 2. (A) TEM images of (Cu, Co, Fe, V, Mn, Pd, Ag, Pt)/SBA-15. (B) The particle distributions of Pd/, Ag/, and Pt/SBA-15 derived from TEM.

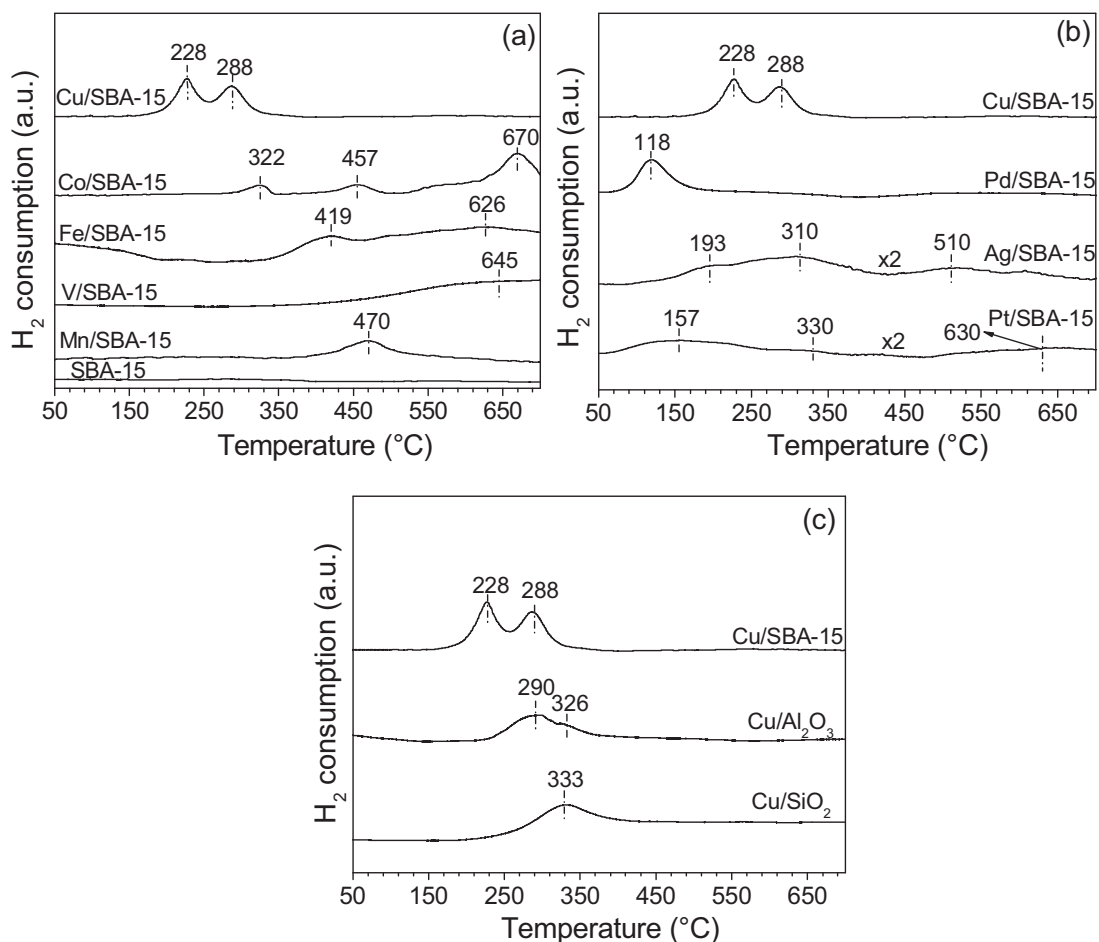


Fig. 3. H₂-TPR profiles of SBA-15 and metal/SBA-15: (a) (Cu, Co, Fe, V, Mn)/SBA-15 with SBA-15 as the reference; (b) (Pd, Ag, Pt)/SBA-15 with Cu/SBA-15 as the reference; (c) Cu/Al₂O₃, Cu/SiO₂ with the Cu/SBA-15 as the reference.

Cu species resulting in more Cu²⁺ cations formed over the surface and exhibiting better redox properties. It is therefore found that SBA-15 could serve as a promising substrate of the copper species for CH₃CN catalytic combustion.

3.3. X-ray photoelectron spectroscopy

For the purpose of better understanding the chemical states and surface compositions of the metallic components over M/SBA-15

Table 2
Quantitative calculation results of the H₂-TPR.

| Sample | Peak position (°C) | Consumption of H ₂ (μmol g ⁻¹) | Total consumption of H ₂ (μmol g ⁻¹) | H/M (μmol μmol ⁻¹) | Total H/M (μmol μmol ⁻¹) |
|-----------------------------------|--------------------|---|---|--------------------------------|--------------------------------------|
| Cu/SBA-15 | 228 | 146.2 | 295.3 | 0.92 | 1.86 |
| | 288 | 149.1 | | 0.94 | |
| Co/SBA-15 | 322 | 33.4 | 413.6 | 0.20 | 2.44 |
| | 457 | 47.8 | | 0.28 | |
| | 670 | 332.4 | | 1.96 | |
| Fe/SBA-15 | 419 | 160.0 | 228.5 | 0.90 | 1.28 |
| | 626 | 68.5 | | 0.38 | |
| V/SBA-15 | 645 | – | 332.5 | – | 1.70 |
| Mn/SBA-15 | 470 | – | 164.2 | – | 0.84 |
| Pd/SBA-15 | 118 | – | 167.8 | – | 1.78 |
| Ag/SBA-15 | 193 | 9.7 | 99.1 | 0.10 | 1.06 |
| | 310 | 63.1 | | 0.68 | |
| | 510 | 26.3 | | 0.28 | |
| Pt/SBA-15 | 157 | 11.1 | 16.3 | 0.22 | 0.32 |
| | 330 | 2.7 | | 0.06 | |
| | 630 | 2.5 | | 0.04 | |
| Cu/Al ₂ O ₃ | 290 | 131.2 | 254.0 | 0.82 | 1.60 |
| | 326 | 122.8 | | 0.78 | |
| Cu/SiO ₂ | 333 | – | 305.8 | – | 1.92 |

Table 3

Surface atomic concentration determined by the XPS.

| Sample | Surface atomic concentration (mol %) | | | $n_M/n_{Si} \times 10^{-2}$ (mol mol ⁻¹) ^b | $n_M/n_{Si} \times 10^{-2}$ (mol mol ⁻¹) ^c |
|-----------------------------------|--------------------------------------|-------|----------------|---|---|
| | Si | O | M ^a | | |
| Cu/SBA-15 | 35.37 | 64.25 | 0.38 | 1.07 | 1.94 |
| Co/SBA-15 | 35.48 | 64.35 | 0.17 | 0.48 | 2.08 |
| Fe/SBA-15 | 35.35 | 64.14 | 0.51 | 1.44 | 2.19 |
| V/SBA-15 | 34.41 | 64.81 | 0.78 | 2.27 | 2.40 |
| Mn/SBA-15 | 35.09 | 64.31 | 0.60 | 1.71 | 2.23 |
| Pd/SBA-15 | 30.78 | 68.94 | 0.28 | 0.91 | 1.16 |
| Ag/SBA-15 | 30.80 | 68.93 | 0.27 | 0.88 | 1.14 |
| Pt/SBA-15 | 31.04 | 68.80 | 0.16 | 0.52 | 0.63 |
| Cu/SiO ₂ | 36.59 | 62.89 | 0.52 | 1.42 | 1.94 |
| – | Al | O | M ^a | $n_M/n_{Al} \times 10^{-2}$ (mol mol ⁻¹) ^b | $n_M/n_{Al} \times 10^{-2}$ (mol mol ⁻¹) ^c |
| Cu/Al ₂ O ₃ | 36.27 | 63.19 | 0.54 | 2.98 | 3.30 |

^a M represents the loaded metals.^b The mole ratio of loaded metal and Si calculated by the XPS.^c The mole ratio of loaded metal and Si calculated by the XRF.

samples as well as Cu/Al₂O₃ and Cu/SiO₂, the XPS were further conducted and with the result being shown in Fig. S1a–i (Supplementary material of XPS investigation section) and Table 3 (surface atomic compositions derived from XPS).

As shown in Fig. S1a the main peak located at 933.2 eV (Cu 2p_{3/2}) combining with its shake-up satellite (941.3 eV) is observed for the Cu/SBA-15, suggesting that the surface copper species are mainly in +2 valence states. Only the Cu²⁺ species (3d⁹) shows a shake-up satellite peak located about 10 eV higher than the Cu 2p_{3/2}. In addition, the isolated cationic Cu²⁺ and the Cu²⁺ in CuO were observed respectively displaying the binding energy (BE) peaked at 945.0 and 941.3 eV [31]. Through comparing the BE peak intensities, the highly dispersed Cu²⁺ ions at 945.0 eV are found to be the main species on the surface of Cu/SBA-15. As for Co/SBA-15 (Fig. S1b), only one intense peak at 781.7 eV (belonging to Co 2p_{3/2}) is observed, which is corresponding to the isolated Co²⁺ cations strongly interacting with the surface of SBA-15 support [32]. As reported [21,33], the Co²⁺/Co³⁺ of Co₃O₄ is located around 780.2 eV, and the Co²⁺ in CoO is centered at 779.5 eV. Therefore, Co²⁺ ions constitute the main cobalt species of Co/SBA-15. The XPS of Fe/SBA-15 exhibits a strong peak at 710.7 eV (Fe 2p_{3/2}) being assigned to the Fe³⁺ ions [34]. The shoulder at 709.0 eV and its satellite at 714.7 eV are attributed to the partially reduced Fe²⁺ ions. Obviously, the Fe³⁺ ions are dominating over Fe/SBA-15. Three BE peaks (641.7, 643.3, and 648.7 eV) were clearly observed for the XPS of Mn/SBA-15, which can be assigned to MnO₂ according to the literature [35]. As for V/SBA-15 only one intense peak at 522.6 eV was observed, which is attributed to the O 1s of the SBA-15 framework. Because the binding energy of V 2p (located around 517 eV) and that of O 1s of V/SBA-15 framework are close to each other, the BE peak of V 2p could be completely masked by the intense one of O 1s, as also reported elsewhere [36]. Based on the above XPS analyses, metallic cations are known to be the major species on the surface of (Cu, Co, Fe)/SBA-15, whereas, the surface of Mn/SBA-15 was mainly covered by metal oxides. This finding is completely consistent with the early H₂-TPR investigations.

The XPS of the noble-metal modified SBA-15 are depicted in Fig. S1f–h. The first peak of Pd/SBA-15 (336.5 eV) being assigned to Pd 3d_{5/2} corresponds to the Pd²⁺ of PdO, and the other one at 342.0 eV is related to Pd 3d_{3/2} [37]. The Ag 3d spectrum of Ag/SBA-15 includes a spin-orbit coupling doublet, 3d_{5/2} (368.0 eV) and 3d_{3/2} (374.2 eV). According to the previous report [38], the peak at 368.0 eV can be assigned to the silver oxide species. As for Pt/SBA-15, one intense peak at 74.5 eV associated with the shoulder of 70.8 eV was observed, which could individually correspond

to PtO and Pt⁰ [27]. Considering the H₂-TPR result of Pt/SBA-15, Pt⁰ being the main species over the surface, the PtO detected by this surface-sensitive XPS probably formed the out-layer of the Pt⁰ cores, resulting in the metallic platinum merely exhibit as an extremely low shoulder at 70.8 eV.

Fig. S1i displays the XPS spectra of Cu supported on Al₂O₃ and SiO₂ with Cu/SBA-15 as a reference. The broad peaks at 933.0 eV associated with the shake-up peaks at 941.2 and 941.8 eV were clearly seen for Cu/Al₂O₃ and Cu/SiO₂, respectively, which reveals that Cu species are mostly in a divalent (+2) state. Their shake-up peaks can also give us a clue that Cu²⁺ species are nearly in the form of CuO on the surfaces of the samples, being in good agreement with those deduced from the H₂-TPR.

Additionally, Table 3 listed the surface atomic compositions of the investigated samples detected by XPS, which were further compared with the related calculation results derived by XRF (n_M/n_{SiO_2} or $n_M/n_{Al_2O_3}$). It can be found that for Cu, Co, and Fe/SBA-15 the values of n_M/n_{SiO_2} calculated by XPS are greatly lower than those calculated by XRF. However, for V, M, Pd, Ag, Pt/SBA-15, Cu/Al₂O₃, and Cu/SiO₂ the related values of n_M/n_{SiO_2} or $n_M/n_{Al_2O_3}$ detected by XPS are similar to those calculated by XRF. This might be explained by that: (I) the loaded metals (Cu, Co, Fe) being mainly in a cationic form transferred into the channels of the SBA-15 where it is hardly detectable by XPS; (II) the metals of V, Mn, Pd, and Ag on SBA-15 and the Cu on Al₂O₃ and SiO₂ are mainly in the form of metal oxides dispersed on the surface of the related substrates, which can be easily detected by means of XPS resulting the value of n_M/n_{SiO_2} or $n_M/n_{Al_2O_3}$ determined by XPS being close to that evaluated by XRF; (III) Pt is mainly in the form of metallic nanoclusters dispersed on the surface of Pt/SBA-15 associated with small fraction of PtO, which is XPS visible. The quantitative analyses of XPS thus confirmed the results of previous characterizations (XRD, TEM, H₂-TPR and XPS).

3.4. Activity test

3.4.1. Activity comparison of 3d TMI modified SBA-15

The temperature dependence on the conversion of CH₃CN as well as the yields of N-containing products (N₂, NO, NO₂, N₂O, NH₃) and C-containing products (CO, CO₂) during CH₃CN catalytic combustion in the presence of oxygen over the parent SBA-15 and 3d TMI (Cu, Co, Fe, V, Mn) supported SBA-15 were investigated and respectively depicted in Fig. 4a–h.

As shown in Fig. 4a, CH₃CN conversion over SBA-15 is marginal at $T < 500$ °C and below 20% at 600–700 °C. Considering about

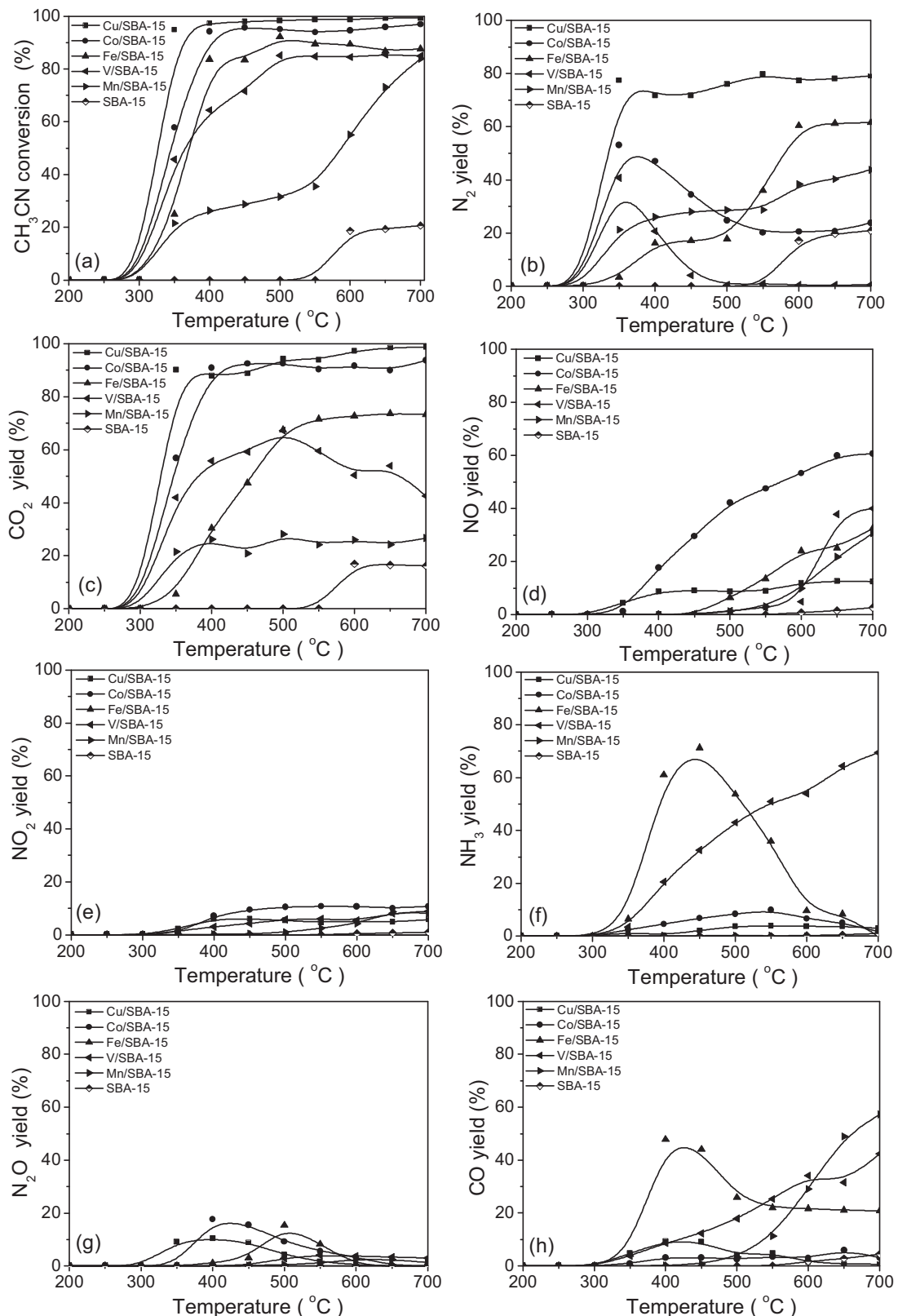


Fig. 4. Catalytic performance as a function of temperature during CH_3CN combustion over SBA-15 and (Cu, Co, Fe, V, Mn)/SBA-15: (a) CH_3CN conversion; (b) N_2 yield; (c) CO_2 yield; (d) NO yield; (e) NO_2 yield; (f) NH_3 yield; (g) N_2O yield; (h) CO yield; Conditions: 1% CH_3CN , 5% O_2 , GHSV = 20,000 h^{-1} .

the chemical inert of lattice oxygen of SBA-15, this nitrile conversion is suspected to be associated with the homogeneous reaction between gaseous CH_3CN and O_2 . Nevertheless, the conversion is significantly improved by the introduction of active

metallic components, wherein Cu/SBA-15 obtains the highest activity with T_{50} (the temperature corresponding to 50% CH_3CN conversion) of 325 °C being lower than those of Co/(340 °C), V/(360 °C), Fe/(370 °C) and Mn/SBA-15 (590 °C). Therefore, it can

be found that the CH_3CN conversions follow a decreasing order of $\text{Cu} > \text{Co} > \text{Fe} > \text{V} > \text{Mn/SBA-15}$.

Apart from CH_3CN conversion being a crucial indicator for evaluating the catalysts performance, the N_2 and CO_2 yields constituting another important evaluation criterion are also important for estimating the catalytic performance due to the possible releasing of other undesirable byproducts (NO , NO_2 , N_2O , NH_3 and CO) during CH_3CN combustion. As shown in Fig. 4b, the N_2 yield of Cu/SBA-15 is significantly higher than those of the other samples under the temperatures above 300°C (77–80%). In contrast, the profiles of $\text{Co}/$ and V/SBA-15 show the large fluctuations with the maximum of 53 and 40% around 400°C , respectively. The related profiles of $\text{Fe}/$ and Mn/SBA-15 display the gradually growing trend with the N_2 yield ranging from 0 to 61.5 and 43.7% at 700°C , respectively. The CO_2 yield profiles depicted in Fig. 4c show that Cu/SBA-15 (90–98%) and Co/SBA-15 (90–93%) possess higher CO_2 selectivities than those of the other samples at $T > 300^\circ\text{C}$.

The undesirable byproducts (NO , NO_2 , N_2O , NH_3 and CO) yields versus temperature for ($\text{Cu, Co, Fe, V, Mn}/\text{SBA-15}$) are respectively depicted in Fig. 4d–h, which are greatly helpful for us to get a deeper insight into the catalytic behaviors of the ($\text{Cu, Co, Fe, V, Mn}/\text{SBA-15}$) samples during CH_3CN catalytic combustion. After carefully analyzing the profiles in Fig. 4d–h, it can be revealed that (I) Cu/SBA-15 possessed high N_2 (77–80%) and CO_2 (90–98%) selectivities as the temperature is higher than 300°C generating only small amount of N_2O , NO_x , and CO ; (II) NO is the main byproducts for Co/SBA-15 growing along with the increase of reaction temperatures and with the maximal value of 60.6% at 700°C ; (III) as for Mn/SBA-15 the NO and CO being of the main byproducts can be formed only at $T > 500^\circ\text{C}$ with the highest values of 30.7% and 57.2% at 700°C , respectively; (IV) NH_3 and CO are readily generated over $\text{Fe}/$ and V/SBA-15 , in which the NH_3 and CO yields of Fe/SBA-15 exhibit a maximum at $\sim 450^\circ\text{C}$ (71.3% and 47.9%, respectively), whereas for V/SBA-15 the NH_3 and CO yields grow along with the temperature achieving the respective maximum values of 69.5% and 42.3% at 700°C ; these findings reveals the different reaction mechanisms were involved for the tested samples, which will be detailedly discussed in Section 3.5.

Based on above analyses it can be found that Cu/SBA-15 not only possessing higher CH_3CN activity but also exhibiting better selectivities toward N_2 and CO_2 is a promising candidate used as a catalyst for CH_3CN selective combustion toward unharful N_2 .

3.4.2. Activity comparison of Cu/SBA-15 with noble-metal modified SBA-15

The catalytic activities of the noble-metal (Pd, Ag, Pt) modified SBA-15 were also evaluated with the results being compared with that of Cu/SBA-15 , as shown in Fig. 5a–h.

As seen from Fig. 5a, except for Ag/SBA-15 ($T_{50} = 435^\circ\text{C}$) displaying a progressively increased CH_3CN conversion upon the rising temperatures, $\text{Pd}/$ or Pt/SBA-15 achieves a better CH_3CN conversion than that of Cu/SBA-15 : the activity sequence according to CH_3CN conversion is of $\text{Pt} > \text{Pd} > \text{Cu} > \text{Ag/SBA-15}$. However, as regard to the N_2 yields (Fig. 5b), the related values of $\text{Pd}/$ and Pt/SBA-15 are seriously suppressed being lower than 30% in the whole tested temperature region. Relatively higher N_2 yield is obtained by Ag/SBA-15 (0–56.5%, $T > 350^\circ\text{C}$). The byproducts yields of ($\text{Pd, Ag, Pt}/\text{SBA-15}$) along with temperature are depicted in Fig. 5d–h, revealing that (I) CH_3CN is mainly converted into NO (72.5% at 700°C) over Pd/SBA-15 , with small amount of N_2O (37.1% at 300°C) formed at lower temperatures (200 – 400°C); (II) N_2O is commonly generated at lower temperatures (200 – 450°C) with a yield as high as 76.4% at 300°C over Pt/SBA-15 (Fig. 5g); upon raising the temperature ($T > 450^\circ\text{C}$) the CH_3CN is rapidly transformed into NO (65% at 700°C); (III) NO generation is totally inhibited in the case of Ag/SBA-15 , resulting in an appearance of NO merely at $T > 450^\circ\text{C}$.

In summary, although the $\text{Pt}/$ and Pd/SBA-15 catalysts exhibited the higher CH_3CN conversions (especially at low temperatures), they predominantly formed the unwanted byproducts of N_2O and NO which belong to the secondarily generated pollutants. Therefore, Cu/SBA-15 exhibiting a nearly complete conversion of CH_3CN at $T > 300^\circ\text{C}$ associated with the perfect N_2 and CO_2 selectivities is confirmed to be an ideal material for the catalytic consumption of CH_3CN .

3.4.3. Activity comparison of Cu supported on the diverse substrates

For the further study, the activities of Cu supported on the different substrates (SBA-15, Al_2O_3 , and SiO_2) with the same Cu loading (2 wt%) for CH_3CN catalytic combustion were also investigated (see Fig. S2a–h). Apparently, Cu supported on SBA-15 exhibits a higher activity as well as better N_2 and CO_2 yields than other carriers, indicating that SBA-15 can serve as the best support of copper species for CH_3CN catalytic combustion. Additionally, it is interestingly noted that NH_3 is more liable to be generated over $\text{Cu/Al}_2\text{O}_3$ during the CH_3CN combustion, especially at 300 – 700°C , showing a yield as high as 100% (see Fig. S2f), while NO_x is more readily formed over Cu/SiO_2 as $T > 300^\circ\text{C}$. This reveals that the CH_3CN conversion likely follows the distinct reaction pathways over Cu catalysts prepared by using the different supports.

3.5. CH_3CN catalytic combustion mechanism based on DRIFTS

3.5.1. DRIFTS of $\text{CH}_3\text{CN} + \text{O}_2$ over Cu/SBA-15

Based on the best performing Cu/SBA-15 (associated with the maximum N_2 yield), the CH_3CN combustion mechanism was further investigated by employing the CH_3CN -DRIFTS, wherein the newly generated surface species during the adsorption of CH_3CN on Cu/SBA-15 at different temperatures were probed, as shown in Fig. 6A. Two vibrational regions can be clearly observed at (2100 – 2500) and (2800 – 3100) cm^{-1} , of which the former one involves the most sensitive spectrum region for the nitriles: the CN stretching mode [$\nu(\text{CN})$, 2100 – 2350 cm^{-1}]. In this $\nu(\text{CN})$ region, a strong doublet at 2260 and 2296 cm^{-1} was clearly observed at low temperatures (150 – 250°C), which corresponds to the Fermi resonance (FR) between the $\text{C}\equiv\text{N}$ stretching and a $\delta\text{CH}_3 + \nu(\text{C}-\text{C})$ combination of the CH_3CN [39]. As noted, a small up-shift (blue shift) is true for these two bands compared with the liquid acetonitrile (AN) (2254 , 2292 cm^{-1}), which is correlated with the electro-withdrawal ability of the cationic sites from the N lone pair upon the adsorption of CH_3CN [40,41]. Considering the coordination chemistry, it is proposed that the AN can be adsorbed on the metal atomic center of the catalyst through two manners: (a) an end-on interaction via the nitrogen lone-pair orbital resulting the $\nu(\text{CN})$ at about 2268 cm^{-1} or a little lower wavenumbers; (b) the side-on interaction via π of $\text{C}\equiv\text{N}$ group having the $\nu(\text{CN})$ of 1734 cm^{-1} [42,43]. It was thus found that the CH_3CN was herein adsorbed on Cu/SBA-15 through its N end according to the DRIFTS data. Another small band at 2323 cm^{-1} is also observed in Fig. 6A, which is related to another $\nu(\text{CN})$ frequency (FR) doublet and with its relatively lower strength being superimposed to the band of 2296 cm^{-1} [39]. Therefore, it can be concluded that these bands at 2296 , 2260 , and 2323 cm^{-1} are all attributed to the chemisorbed CH_3CN on Cu/SBA-15 .

As the temperature rose up, the band intensity of $\nu(\text{CN})$ (2260 , 2296 and 2323 cm^{-1}) gradually decreased with only one band at 2296 cm^{-1} left at $T > 250^\circ\text{C}$. Simultaneously, another band at 2198 cm^{-1} was newly generated at 300°C . Raskó and Kiss [44] previously investigated the adsorption and catalytic elimination of acetonitrile over Rh supported TiO_2 finding that CH_3CN could be firstly dissociated into $\text{CN}_{(\text{a})}$ (the CN adsorbed on the catalyst)

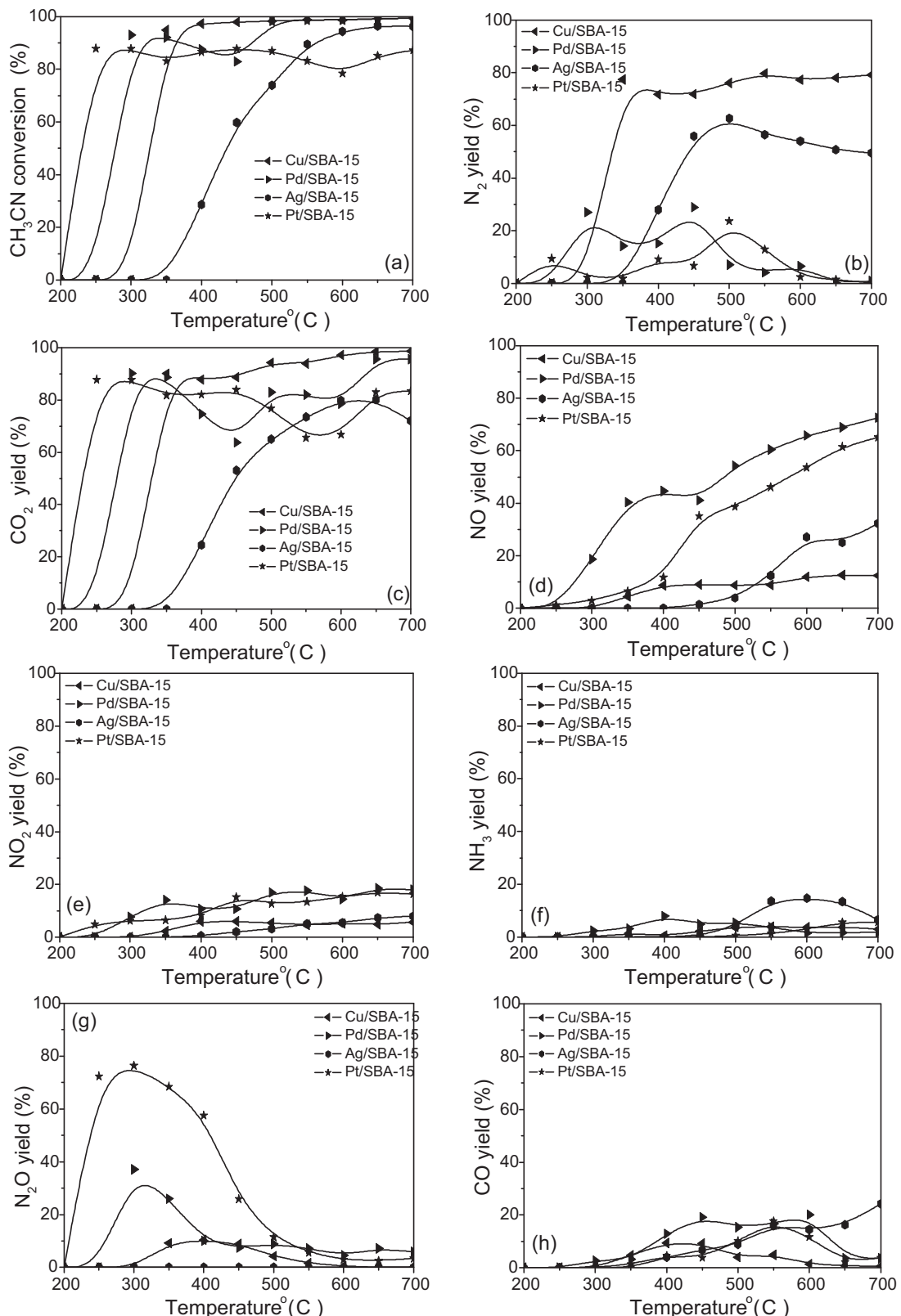


Fig. 5. Catalytic performance as a function of temperature during CH₃CN combustion over (Pd, Ag, Pt)/SBA-15: (a) CH₃CN conversion; (b) N₂ yield; (c) CO₂ yield; (d) NO yield; (e) NO₂ yield; (f) NH₃ yield; (g) N₂O yield; (h) CO yield; Conditions: 1% CH₃CN, 5% O₂, GHSV = 20,000 h⁻¹.

and successively oxidized into the surface isocyanide (NCO) species which displayed IR spectra around 2200–2210 cm⁻¹. Additionally, the NCO being of an important intermediate is also widely reported in selective catalytic reduction of NO (SCR). London and Bell [45]

ascribed a band at 2200 cm⁻¹ to copper isocyanide (Cu⁺NCO⁻) during the reduction of nitric oxide by carbon monoxide over copper oxide. In our previous work [46] of the infrared mechanism study on catalytic reduction of NO by CO over Cu/Ce_xZr_{1-x}O₂, a

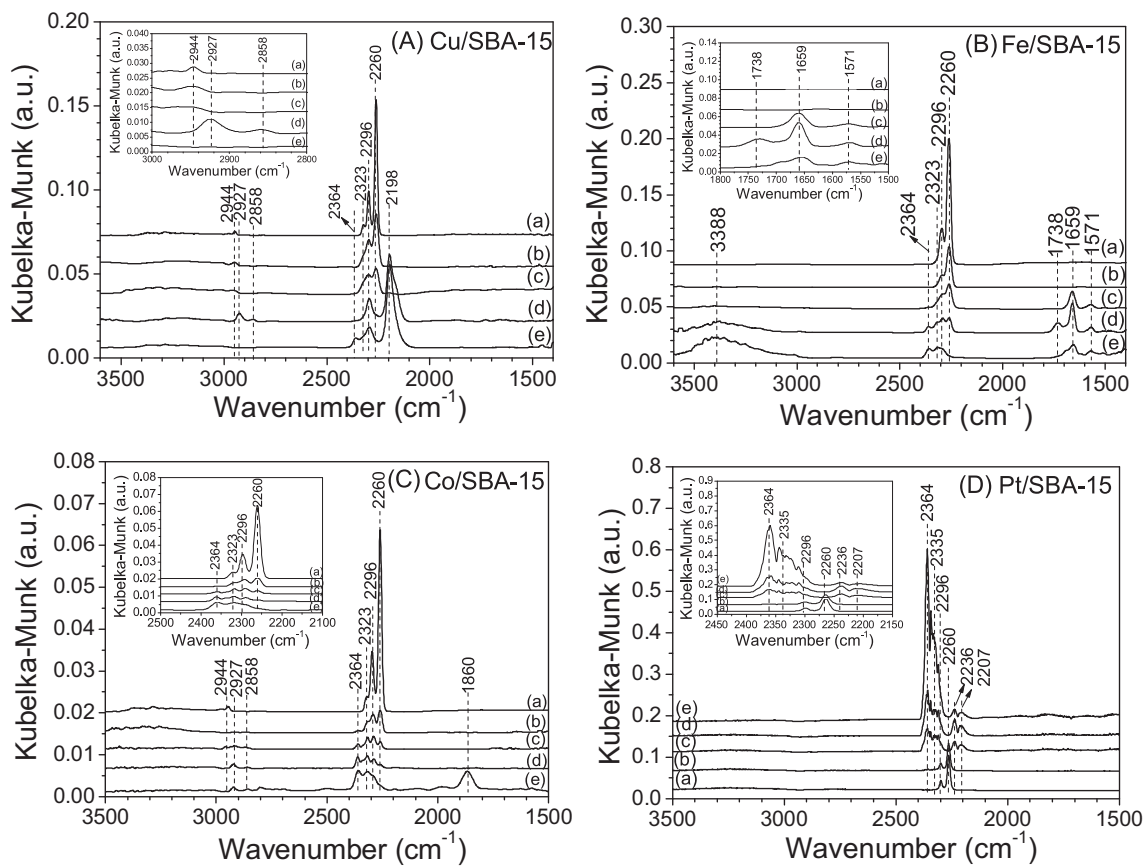


Fig. 6. DRIFTS of adsorbates produced from the flow of CH_3CN (1 vol%) + O_2 (5 vol%) + He (94 vol%) for 10 min over (A) Cu/SBA-15; (B) Fe/SBA-15; (C) Co/SBA-15; (D) Pt/SBA-15: at (a) 150 °C; (b) 200 °C; (c) 250 °C; (d) 300 °C; and (e) 350 °C; the total flow rate is 20 ml min⁻¹ (STP).

relatively broad band at 2190–2280 cm^{-1} was achieved, which was also ascribed to the NCO of $\text{Cu}^{+}\text{-NCO}$. In the light of above literature reports, we can accordingly assign the band of 2198 cm^{-1} in Fig. 6A to the NCO vibration of $\text{Cu}^{+}\text{-NCO}$.

The bands in the other region of 2800–3100 cm^{-1} correspond to the vibrations of CH [$\nu(\text{CH})$] [47]. Through infrared analysis on $\nu(\text{CH})$, some important information can also be obtained. As noted, at the lower temperatures (150–250 °C) only the band of 2944 cm^{-1} can be observed, which is attributed to the $\nu(\text{CH})$ of adsorbed CH_3CN . As the temperature rose reaching 300 °C, two new bands at 2858 and 2927 cm^{-1} were generated, whereas the band of 2944 cm^{-1} vanished. Combing with the observation that the NCO was also generated at 300 °C (2198 cm^{-1}) and the literature report that the prerequisite of NCO formation was the dissociation of CH_3CN (C–C bond breakage) [47], the newly generated bands at 2858 and 2927 cm^{-1} can be assigned to the $\nu(\text{CH})$ of $\text{CH}_{3(a)}$ formed by the C–C bond fracture of $\text{CH}_3\text{-CN}$ molecule. Then, the generated $\text{CN}_{(a)}$ is readily oxidized to NCO under the oxygen-rich condition (5 vol% O_2) of the present work. Along with the further temperature increase up to 350 °C, the $\nu(\text{CH})$ bands at 2858 and 2927 cm^{-1} totally diminished, whereas another band at 2364 cm^{-1} , being attributed to CO_2 , was generated. It is known that the formed $\text{CH}_{3(a)}$ is finally oxidized into CO_2 at the elevated temperatures.

Based on the above analyses, CH_3CN combustion mechanism over Cu/SBA-15 can be concluded as follows and also shown in **Scheme 1**: (I) the CH_3CN can be firstly adsorbed on Cu/SBA-15 through its N end at lower temperatures (Reaction step 1); (II) as the temperature rises up ($T > 250$ °C), the $\text{CH}_3\text{-CN}$ bond begins to fracture forming the adsorbed $\text{CH}_{3(a)}$ and $\text{CN}_{(a)}$ (Reaction step 2A); (III) the $\text{CN}_{(a)}$ can be readily oxidized into the NCO through Reaction step 3A(a) which is thought as an important step for CH_3CN combustion;

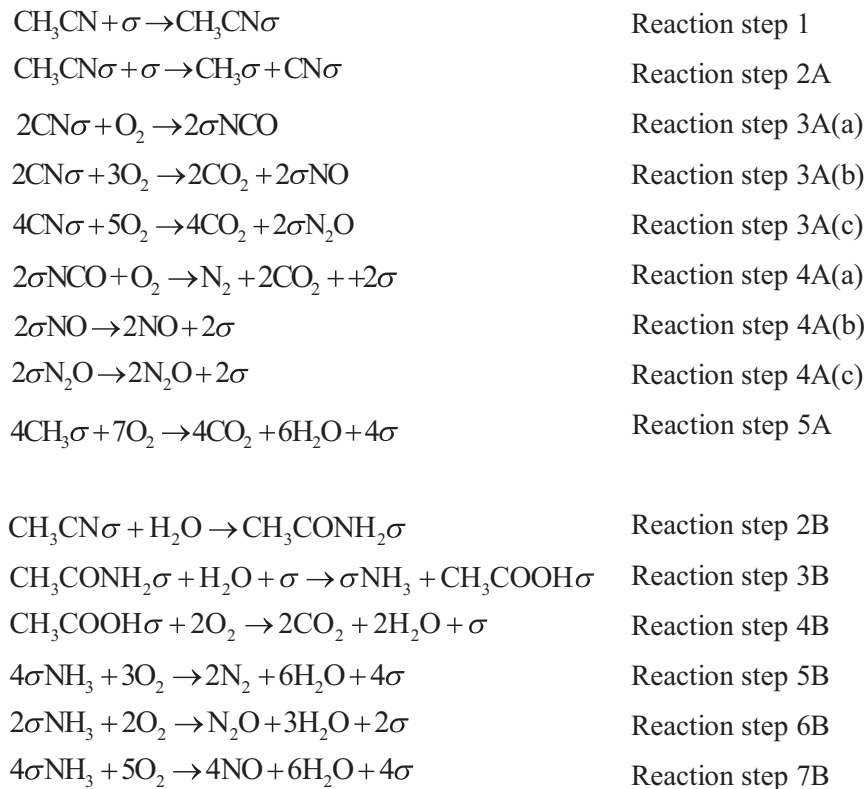
(IV) the following Reaction step of 4A(a) represents a selective oxidation of the NCO intermediate forming N_2 and CO_2 ; (V) the $\text{CH}_{3(a)}$ can be further oxidized into CO_2 at $T > 300$ °C (Reaction step 5A), as also found during the activity evaluations of Fig. 4c.

3.5.2. DRIFTS of $\text{CH}_3\text{CN} + \text{O}_2$ over Fe/SBA-15

Due to the special behavior of Fe/SBA-15 during the CH_3CN catalytic combustion forming large amount of NH_3 , we also investigated the corresponding combustion mechanism taking place over Fe/SBA-15 based on the infrared technique, as illustrated in Fig. 6B, wherein the experimental procedures for DRIFTS study are similar to those of Cu/SBA-15.

As shown in Fig. 6B, two extensive bands at 2260 and 2296 cm^{-1} (including the shoulder of 2323 cm^{-1}) are clearly observed at 150 °C due to the $\nu(\text{CN})$ of the chemisorbed CH_3CN , implying that the CH_3CN is also adsorbed on the Fe/SBA-15 through its N end. At the elevated temperatures, these bands progressively decreased associated with some new bands of 1571, 1659, 1738, 2364, and 3388 cm^{-1} appearing ($T > 200$ °C). According to the literature reports the broad band centered at 3388 cm^{-1} is attributed to the adsorbed NH_x species ($1 < x < 3$) [48]; the band at 2364 cm^{-1} is assigned to CO_2 ; the band of 1738 cm^{-1} represents the C=O vibrations [$\nu(\text{C=O})$] of acetic acid [49]; and the bands of 1571, 1658 cm^{-1} are correlated with the acetamide species [50]. IR spectra of Fe/SBA-15 with the absence of band for the isocyanide (NCO) species (Fig. 6B) are greatly distinguishing from those of Cu/SBA-15 (Fig. 6A), revealing a combustion mechanism different from that proposed for Cu/SBA-15 occurs over Fe/SBA-15, as detailedly discussed below.

Through above IR investigation for Fe/SBA-15, it is confirmed that the acetamide is generated at 250 °C displaying the



σ represents the active site of the supported metal catalyst

Scheme 1. CH_3CN combustion mechanism over the supported metal catalyst during DFT calculations.

IR bands at 1571 and 1659 cm^{-1} , which is likely due to the hydrolysis of the chemisorbed CH_3CN following the reaction of $\text{CH}_3\text{CN} + \text{H}_2\text{O} \rightarrow \text{CH}_3\text{CONH}_2$. With the temperature increased up to 300°C , the bands of acetamide ($1571, 1659\text{ cm}^{-1}$) slightly grew up, accompanying with the generations of new bands of NH_x (3388 cm^{-1}), acetic acid (1738 cm^{-1}), and CO_2 (2364 cm^{-1}). These findings suggest that (I) at this temperature (300°C) the CH_3CN is able to be hydrolyzed into acetamide, leading to an enhancement in the related bands ($1571, 1659\text{ cm}^{-1}$); (II) the generated acetamide can be further hydrolyzed to produce the acetic acid and NH_3 ; (III) small amount of CO_2 is generated by the oxidation of acetic acid. Similar results were also announced by Nanba et al. [48] during the investigation of $\text{C}_2\text{H}_3\text{CN}$ catalytic purification over Ag catalyst, in which they pointed out that the elimination of $\text{C}_2\text{H}_3\text{CN}$ over Ag/TiO_2 followed a hydrolysis pathway forming the acrylamide, acrylic acid and NH_x species.

Upon heating to 350°C , the bands of acetamide ($1571, 1659\text{ cm}^{-1}$) and acetic acid (1738 cm^{-1}) decreased to a large extent, whereas the band intensities of NH_x (3388 cm^{-1}) and CO_2 (2364 cm^{-1}) increased. On the basis of these observations, it is deduced that at 350°C the formed acetamide is mostly hydrolyzed into the NH_x and acetic acid, of which the latter one is thereafter directly oxidized to CO_2 and H_2O resulting in the disappearance of the band of acetic acid (1738 cm^{-1}). Additionally, it is also worth noting that small amount of the acetamide still can be observed at 350°C , suggesting the strong stability of the acetamide on the surface of Fe/SBA-15, which probably can poison the active sites of Fe/SBA-15 and reduce the total activity of Fe/SBA-15 for CH_3CN catalytic combustion.

Due to the limitation of our infrared instrument, we cannot conduct the further DRIFTS investigations at extremely higher temperatures ($T > 350^\circ\text{C}$). However, the activity data showing in

Fig. 4a–h, derived from the off-gas analyses by infrared gas analyzer, can help us to complement CH_3CN combustion mechanism over Fe/SBA-15. As shown in Fig. 4f, large amount of NH_3 was generated over Fe/SBA-15 achieving the maximum NH_3 yield as high as 71.4% at 450°C in the temperature range of $350\text{--}450^\circ\text{C}$, indicating that CH_3CN was greatly hydrolyzed into the NH_3 at this temperature range. Meanwhile, the generation of N_2 with a yield of 17.1% at 450°C and small amount of N_2O was also testified, which is attributed to the selective oxidation of NH_3 over Fe/SBA-15. As $T > 450^\circ\text{C}$, the NH_3 yield decreased rapidly with a drop nearly closed to zero at $T > 600^\circ\text{C}$ (see Fig. 4f) combining with a remarkably growing of N_2 and small amount of NO and N_2O generated. These findings further imply that NH_3 generated by the hydrolysis of CH_3CN follows a selective oxidation mechanism at $T > 450^\circ\text{C}$, in which the NH_3 is mainly oxidized into N_2 with small amount of NO and N_2O generated as the byproducts.

In order to give the further evidence, NH_3 selective oxidation was conducted over Fe/SBA-15, as shown in Fig. S3 (see Supplementary material). It is confirmed that NH_3 can be selectively oxidized into N_2 (as the main product) over Fe/SBA-15 associated with small amount of NO . In addition to that, the initial temperature ($T > 300^\circ\text{C}$) for NH_3 conversion is found to be similar to the initial temperature for N_2 generation during CH_3CN combustion over Fe/SBA-15 (Fig. 4b). These findings confirm that N_2 generated during CH_3CN combustion over Fe/SBA-15 is essentially attributed to the selective oxidation of NH_3 .

Therefore, the CH_3CN catalytic combustion mechanism over Fe/SBA-15 can be summarized in two steps: the initial hydrolysis of CH_3CN into ammonia followed by the selective oxidation of the generated NH_3 . The related mechanism scheme is formulated by Reaction steps 2B–7B in Scheme 1.

3.5.3. DRIFTS of $\text{CH}_3\text{CN} + \text{O}_2$ over Co/SBA-15

Fig. 6C shows the DRIFTS of $\text{CH}_3\text{CN} + \text{O}_2$ over Co/SBA-15, which exhibited a relatively higher selectivity toward NO during CH_3CN combustion (see **Fig. 4d**), with an aim to reveal the related mechanism. As noted, similar to that of Cu/SBA-15, CH_3CN is able to be adsorbed upon Co/SBA-15 displaying the $\nu(\text{CN})$ bands of 2260, 2296, and 2323 cm^{-1} as well as the $\nu(\text{CH})$ band (2944 cm^{-1}) at 150°C . At the rising temperatures in the region of $200\text{--}300^\circ\text{C}$, small amount of CO_2 was generated with an infrared band of 2364 cm^{-1} being gradually increased, whereas IR bands of the chemisorbed CH_3CN are decreased. According to the assignment for Cu/SBA-15 (Section 3.5.1), the bands of 2858 and 2927 cm^{-1} are owing to the $\nu(\text{CH})$ of $\text{CH}_{3(a)}$ formed by a C-C bond fracture of $\text{CH}_3\text{-CN}$ molecule. These two bands are also observed for Co/SBA-15 (Profile d of **Fig. 6C**), indicating that the adsorbed CH_3CN begins to decompose over Co/SBA-15 at $T > 300^\circ\text{C}$. With the temperature increase reaching 350°C , a new band at 1860 cm^{-1} was distinguished, which can be attributed to the adsorbed NO species upon Co^{2+} ions [51]. Obviously, this is different from that of Cu/SBA-15, of which the NCO is generated during the DRIFTS investigations under the same conditions. It is speculated that the different catalytic behaviors between Cu/SBA-15 and Co/SBA-15 are mainly attributed to their distinctly oxidative properties. Due to the strong oxidation ability of Co/SBA-15, the CH_3CN can be directly oxidized into NO without the obvious appearance of NCO intermediate. The CH_3CN catalytic combustion mechanism for Co/SBA-15 generally follows the reaction pathway of Reaction step 3A(b)–Reaction Step 4A(b) yielding large amount of NO, as also revealed by the activity evaluation of **Fig. 4d**.

3.5.4. DRIFTS of $\text{CH}_3\text{CN} + \text{O}_2$ over Pt/SBA-15

As seen from **Fig. 6D**, the $\nu(\text{CN})$ bands of 2260 and 2296 cm^{-1} over Pt/SBA-15 are again observed at the lower temperatures (150 and 200°C). As soon as the temperature increases up to 250°C , these $\nu(\text{CN})$ bands totally vanished simultaneously with a generation of some new bands at 2335 and 2364 cm^{-1} (corresponding to CO_2) as well as 2207 and 2236 cm^{-1} (being attributed to N_2O) [52]. This finding is also consistent with the activity tests: CO_2 (**Fig. 5c**) and N_2O (**Fig. 5g**) are largely formed at $T > 250^\circ\text{C}$ along with a CH_3CN conversion achieving nearly 90% (**Fig. 5a**). Accordingly, it is realized that CH_3CN oxidation mechanism for Pt/SBA-15 is also different from those for Cu, and Co/SBA-15, wherein the CH_3CN is preferably oxidized into N_2O at $T < 350^\circ\text{C}$. Due to the experimental limitation, no further DRIFTS investigation could be conducted at $T > 350^\circ\text{C}$. However, based on the activity data in **Fig. 5d**, NO yield becomes significant at $T > 350^\circ\text{C}$. Therefore, the related mechanism for Pt/SBA-15 likely involves a reaction pathway of Reaction step 3A(c)–Reaction step 4A(c) in favor of N_2O generation at the low-temperature region ($200\text{--}350^\circ\text{C}$) mainly generating N_2O , and Reaction step 3A(b)–Reaction step 4A(b) readily forming NO at the higher temperatures ($T > 350^\circ\text{C}$).

3.5.5. Mechanism assignment

As reported [9], Kröcher and Elsener proposed two kinds of mechanism based on the diverse performances of the investigated catalysts during HCN catalytic removal: (I) for the “oxidation mechanism”, N_2 and CO_2 are the main products simultaneously with N_2O , NO_x and CO as the byproducts; (II) for the “hydrolysis mechanism”, the NH_3 , CO , and H_2O are commonly generated. In the present DRIFTS study, these two kinds of combustion mechanisms were respectively verified with respect to Cu/SBA-15 and Fe/SBA-15 for CH_3CN catalytic combustion. In addition to that, another two kinds of complementary mechanisms with the “NO formation” for Co/SBA-15 and “ N_2O formation” for Pt/SBA-15 were herein proposed. Thereafter, the presently investigated catalysts could be commonly classified into four groups according to the

proposed mechanisms and the related reaction selectivities, as listed in **Table 4**. For the purpose of better description, in this study, the oxidation mechanism with N_2 as the main product is renamed as a “ N_2 formation” mechanism; and the hydrolysis mechanism is noted as a “ NH_3 formation” mechanism.

In summary, the nitrile combustion occurring over Cu, Mn and Ag/SBA-15 follows a “ N_2 formation” mechanism; while those combustions taking place over Fe, V/SBA-15 and Cu/Al₂O₃ perhaps involve a “ NH_3 formation” mechanism. Moreover, Co/SBA-15 and Cu/SiO₂ are attributed to a “NO formation” mechanism; and both the “ N_2O formation” mechanism (at lower temperatures) and “NO formation” mechanism (at higher temperatures) are included for Pt, Pd/SBA-15.

3.6. Correlation between physicochemical properties and catalytic performance

3.6.1. 3d TMI (Cu, Co, Fe, V, Mn) modified SBA-15

Since the parent SBA-15 is proven to be inactive for CH_3CN combustion in the presence of oxygen, the loaded metallic components are believed to act as the active sites, resulting in an obvious enhancement in CH_3CN conversion (**Figs. 4a and 5a**). The characterizations of local structure and coordination environment of active sites were conducted by XRD (**Fig. 1**), H₂-TPR (**Fig. 3**), and XPS (**Fig. S1**). It was found that the metals of Cu, Co, and Fe were mainly distributed over the SBA-15 substrate as the metallic cations; however, the metal oxides were confirmed to be the dominating species for V and Mn/SBA-15 samples probably resulting in the poor activities of Mn and V/SBA-15 for CH_3CN catalytic combustion as compared to the other samples. As reported [3], the metal ions being verified to be the most active site for the $\text{C}_2\text{H}_3\text{CN}$ removal exhibited higher activity, whereas relatively the worse activity was found for their deriving oxides. In addition to that, the H₂-TPR is conducted to further evaluate the redox abilities of the M/SBA-15 samples, which indicated that except for Mn and V/SBA-15 the redox ability of M/SBA-15 (Cu > Co > Fe > Mn > V/SBA-15) is in good agreement with the CH_3CN conversion (Cu > Co > Fe > V > Mn/SBA-15). Therefore, it can be found that the activity differences of the investigated 3d TMI modified SBA-15 samples during CH_3CN catalytic combustion are essentially correlated with the redox abilities of the loaded metals species.

As stated above, for Fe, V/SBA-15, CH_3CN combustion followed the NH_3 mechanism (**Scheme 1**, Reaction step 2B–Reaction step 7B). The redox abilities of these samples played important roles in this kind of mechanism, especially in NH_3 selective oxidation and CH_3COOH oxidation processes. As inferred from H₂-TPR result, Fe/SBA-15 exhibited better redox ability than that of V/SBA-15, which could result in the higher NH_3 and CH_3COOH oxidation rates of Fe/SBA-15 than those of V/SBA-15. Therefore, Fe/SBA-15 exhibited higher final CH_3CN conversion. As shown in **Fig. 4d**, NH_3 yield of Fe, V/SBA-15 increased with the temperature at $T < 400^\circ\text{C}$. However, it decreased to a large extent at $T > 400^\circ\text{C}$ for Fe/SBA-15 mainly forming large amount of N_2 , which is attributed to the superior redox ability of Fe/SBA-15. On the contrary, a continuous increase of NH_3 yield was found for V/SBA-15 with relatively low redox ability as $T > 400^\circ\text{C}$.

An attempt to correlate the selectivities of the (Cu, Co, Fe, V, Mn)/SBA-15 during CH_3CN catalytic combustion with both the redox abilities and chemical natures of the loaded metals has also been done in the present study. As for Cu/SBA-15 the CH_3CN is mainly transformed to N_2 likely due to its ideal redox properties of $\text{Cu}^{2+} \rightarrow \text{Cu}^+$. As reported [3], the square-planar Cu^{2+} ions on Cu/ZSM-5 are found to be the most active site in the catalytic conversion of $\text{C}_2\text{H}_3\text{CN}$ to N_2 due to an easy $\text{Cu}^{2+} \leftrightarrow \text{Cu}^+$ transformation. Similar performance of Cu/ZSM-5 was also reported during HCN catalytic purification exhibiting the high catalytic activity and

Table 4

Mechanism assignment for the investigated samples.

| Mechanism | “N ₂ formation” mechanism | “NH ₃ formation” mechanism | “NO formation” mechanism | “N ₂ O formation” mechanism |
|-----------|--------------------------------------|--|--|--|
| Sample | Cu/SBA-15 Mn/SBA-15 Ag/SBA-15 | Fe/SBA-15 V/SBA-15 Cu/Al ₂ O ₃ | Co/SBA-15 Cu/SiO ₂ Pd/, Pt/SBA-15 | Pd/, Pt/SBA-15 |

N₂ selectivity [9]. However, for Co/SBA-15 NO is the main product during CH₃CN combustion, perhaps being related to the strong oxidation ability of Co/SBA-15. Owing to the poor redox ability, Mn/SBA-15 exhibited the worst activity for CH₃CN catalytic combustion mostly generating N₂ associated with the byproducts of NO and CO only at $T > 500$ °C. As for the Fe/, V/SBA-15, the reaction products were distinct from those of Cu/, Co/, and Mn/SBA-15 yielding large amounts of NH₃, which can be attributed to the special chemical natures of the loaded Fe and V species.

3.6.2. Noble-metal (Pd, Ag, Pt) modified SBA-15

As for the noble metal promoted SBA-15, the metal oxides are confirmed to be the main species for Pd/, Ag/SBA-15 and the metal clusters being of the main species on Pt/SBA-15. The related activity with the Cu/SBA-15 as a reference (Pt/ > Pd/ > Cu/ > Ag/SBA-15) is also found to be consistent with their oxidation ability (Pd/ ≈ Pt/ > Cu/ > Ag/SBA-15), revealing the redox properties greatly influence the activities of (Pd, Ag, Pt)/SBA-15 during CH₃CN conversion. Additionally, the redox abilities can also determine the selectivities of (Pd, Ag, Pt)/SBA-15. Due to the strong oxidation ability of Pd/SBA-15, CH₃CN is largely oxidized into NO with small amount of N₂O generated at the lower temperatures (200–400 °C). Similarly, N₂O becomes the main byproduct at lower temperatures (200–400 °C) and the NO can only be greatly formed at $T > 400$ °C for Pt/SBA-15 sample. The Ag/SBA-15 exhibits the lowest redox ability, resulting in that CH₃CN conversion starts at the temperatures higher than 350 °C, and only small amount of NO (32.3% at 700 °C) was formed at $T > 450$ °C.

3.6.3. Cu supported on the diverse substrates (SBA-15, Al₂O₃, SiO₂)

The activity comparisons among the Cu supported on different substrates reveal that Cu/SBA-15 is superior to the other investigated samples (Cu/Al₂O₃ and Cu/SiO₂). This is firmly attributed to the special structure topology of SBA-15. The mesoporous structure of SBA-15 possessing the long-distance ordering and satisfactory surface areas (around 400–650 m² g⁻¹) facilitates the metal dispersions, which results in the highly dispersed Cu²⁺ ions being the main species over Cu/SBA-15 displaying the higher CH₃CN conversion and the excellent N₂ selectivity. Differently, the CuO exists as the main species over Cu/Al₂O₃ (312 m² g⁻¹) and Cu/SiO₂ (324 m² g⁻¹) resulting in the relatively poor CH₃CN activity and N₂ selectivity.

The selectivity analyses on Cu/Al₂O₃ and Cu/SiO₂ during CH₃CN catalytic combustion reveal that the distinct reaction pathways were involved for Cu/Al₂O₃ (“NH₃ formation” mechanism) and Cu/SiO₂ (“NO formation” mechanism), which is mainly attributed to the different properties of the supports. As reported [53], the Al₂O₃ could be used to hydrolyze the HCN in oxygen-free off-gas streams at 400 °C generally forming NH₃, which was believed to be a practical method for the removal of HCN from the coal gas. Nevertheless, it should also be noted that the loaded metals could further influence the performances of Al₂O₃. Due to the strong oxidizing property of the loaded Pt species, the Pt/Al₂O₃ was deemed as a suitable oxidation catalyst for HCN elimination to individually generate NO_x, N₂, N₂O, CO₂, and H₂O [7]. In light of these literature reports we can deduce that during CH₃CN conversion in the presence of O₂ over Cu/Al₂O₃ the substrate of Al₂O₃ not only can participate into the combustion process but also play an

important role on inducing the reaction to fulfill with a “NH₃ formation” mechanism.

As for the CH₃CN conversion over Cu/SiO₂, only the CuO species can participate into the nitrile transformation, because the chemical property of SiO₂ is similar to that of SBA-15 which hardly displays any activity for CH₃CN conversion (see Fig. 4a). As also found in Ref. [7], the SiO₂ showed no obvious HCN elimination activity. Thus, the activity and selectivity during CH₃CN catalytic combustion over Cu/SiO₂ are certainly related to the loaded metal species (CuO). Nanba et al. [3] investigating the activity of the CuO/SiO₂ for C₂H₃CN catalytic combustion proposed that NO_x were easily formed as temperatures being above 350 °C. This is similar to that found in present work during CH₃CN catalytic combustion over Cu/SiO₂, revealing that the CH₃CN conversion over this sample mainly follows a “NO formation” mechanism.

4. Conclusions

In summary, a series of mono-functional M/SBA-15 [M=transition metals (Cu, Co, Fe, V, Mn) and noble metals (Pd, Ag, Pt)] catalysts was prepared via a transitional impregnation method and applied for CH₃CN catalytic combustion. CH₃CN conversions achieving over the investigated catalysts follow a trend of Pt/ > Pd/ > Cu/ > Co/ > Fe/ > V/ > Ag/ > Mn/ > SBA-15, being correlated well with the redox abilities of M/SBA-15. The selectivities of M/SBA-15, being another crucial standard for evaluating the catalytic performance during CH₃CN purification, are determined by both the redox abilities of M/SBA-15 and the chemical natures of the loaded metal species. Among the prepared M/SBA-15 samples, Cu/SBA-15 exhibited a nearly complete CH₃CN conversion associated with a N₂ selectivity of around 80% at $T > 350$ °C, being regarded as a promising material for catalytic removal of nitrile gases. Finally, four kinds of reaction mechanisms for CH₃CN catalytic combustion were proposed based on DRIFTS studies [namely, “N₂ formation” mechanism for Cu/, Mn/ and Ag/SBA-15, “NH₃ formation” mechanism for Fe/, V/SBA-15 and Cu/Al₂O₃, “N₂O formation” for Pt/, Pd/SBA-15 (at low temperature), “NO formation” mechanism for Co/SBA-15 and Cu/SiO₂ as well as for Pt/, Pd/SBA-15 (at high temperature)].

Acknowledgments

The authors thank the National Natural Science Foundation of China under Grant (Nos. 20977004, 21177008, and 21121064), National “863” project (No. 2013AA065901), and the New Century Program for Excellent Talents in University (NCET-10-0204) for the financial support.

Appendix A. Supplementary data

Supplementary data associated with this article can be found, in the online version, at <http://dx.doi.org/10.1016/j.apcatb.2013.03.028>.

References

[1] P. Dagaut, P. Glarborg, M.U. Alzueta, *Progress in Energy and Combustion Science* 34 (2008) 1–46.

[2] J. Giménez-López, A. Millera, R. Bilbao, M.U. Alzueta, *Combustion and Flame* 157 (2010) 267–276.

[3] T. Nanba, S. Masukawa, A. Ogata, J. Uchisawa, A. Obuchi, *Applied Catalysis B* 61 (2005) 288–296.

[4] T.W. Asmus, T.J. Houser, *Journal of Physical Chemistry* 73 (1969) 2555–2558.

[5] T. Miyadera, *Applied Catalysis B* 16 (1998) 155–164.

[6] F. Solymosi, L. Bugyi, *Surface Science* 147 (1984) 685–701.

[7] H. Zhao, R.G. Tonkyn, S.E. Barlow, B.E. Koel, C.H.F. Peden, *Applied Catalysis B* 65 (2006) 282–290.

[8] X. Guo, A. Winkler, I. Chorkendorff, P.L. Hagans, H.R. Siddique, J.T. Yates Jr., *Surface Science* 203 (1988) 17–32.

[9] O. Kröcher, M. Elsener, *Applied Catalysis B* 92 (2009) 75–89.

[10] Y. Li, J.N. Armor, *Applied Catalysis B* 13 (1997) 131–139.

[11] T. Nanba, S. Masukawa, J. Uchisawa, A. Obuchi, *Journal of Molecular Catalysis A: Chemical* 276 (2007) 130–136.

[12] I.O.Y. Liu, N.W. Cant, *Journal of Catalysis* 195 (2000) 352–359.

[13] F. Solymosi, J. Kiss, *Surface Science* 108 (1981) 368–380.

[14] D. Zhao, J. Feng, Q. Huo, N. Melosh, G.H. Fredrickson, B.F. Chmelka, G.D. Stucky, *Science* 279 (1998) 548–552.

[15] R. Zhang, D. Shi, Y. Zhao, B. Chen, J. Xue, X. Liang, Z. Lei, *Catalysis Today* 175 (2011) 26–33.

[16] Y. Cao, R. Zhang, B. Chen, *Chemical Journal of Chinese Universities* 32 (2011) 2849–2855.

[17] S. Yuvaraj, T. Chang, C. Yeh, *Journal of Catalysis* 221 (2004) 466–473.

[18] V. Hoang, Q. Huang, M. Eić, T. Do, S. Kaliaguine, *Langmuir* 21 (2005) 2051–2057.

[19] C. Toree-Abreu, M.F. Ribeiro, C. Henriques, G. Delahay, *Applied Catalysis B* 12 (1997) 249–262.

[20] P. Arnoldy, J.A. Moulijn, *Journal of Catalysis* 93 (1985) 38–54.

[21] A. Martínez, C. López, F. Márquez, I. Díaz, *Journal of Catalysis* 220 (2003) 486–499.

[22] R. Zhang, A. Villanueva, H. Alamdar, S. Kaliaguine, *Journal of Catalysis* 237 (2006) 368–380.

[23] G. Wang, S. Zhang, Y. Huang, F. Kang, Z. Yang, Y. Guo, *Applied Catalysis A* 413–414 (2012) 52–61.

[24] A. De Lucas, J.L. Valverde, F. Dorado, A. Romero, I. Asencio, *Journal of Molecular Catalysis A: Chemical* 225 (2005) 47–58.

[25] F. Yin, S. Ji, P. Wu, F. Zhao, C. Li, *Journal of Catalysis* 257 (2008) 108–116.

[26] X. Zhang, Z. Qu, X. Li, Q. Zhao, Y. Wang, X. Quan, *Catalysis Communications* 16 (2011) 11–14.

[27] A.K. Medina-Mendoza, M.A. Cortés-Jácomeb, J.A. Toledo-Antoniob, C. Angeles-Chávez, E. López-Salinas, I. Cuauhtémoc-López, M.C. Barrera, J. Escobar, J. Navarrete, I. Hernández, *Applied Catalysis B* 106 (2011) 14–25.

[28] S.C. Shen, S. Kawi, *Applied Catalysis B* 45 (2003) 63–76.

[29] D.L. Hang, T.T.H. Dang, J. Engeldinger, M. Schneider, J. Radnik, M. Richter, A. Martin, *Journal of Solid State Chemistry* 184 (2011) 1915–1923.

[30] T. Nanba, S. Masukawa, J. Uchisawa, A. Obuchi, *Catalysis Letters* 93 (2004) 195–201.

[31] J. Batista, A. Pintar, D. Mandrino, M. Jenko, V. Martin, *Applied Catalysis A* 206 (2001) 113–124.

[32] H. Cui, Y. Zhang, Z. Qiu, L. Zhao, Y. Zhu, *Applied Catalysis B* 101 (2010) 45–53.

[33] L. Guzzi, D. Bazin, *Applied Catalysis A* 188 (1999) 163–174.

[34] J. Yamashita, P. Hayes, *Applied Surface Science* 254 (2008) 2441–2449.

[35] M.C. Biesinger, B.P. Payne, A.P. Grosvenor, L.W.M. Lau, A.R. Gerson, R.St.C. Smart, *Applied Surface Science* 257 (2011) 2717–2730.

[36] M. Faraldo, J.A. Anderson, M.A. Banares, J.L.G. Fierro, S.W. Weller, *Journal of Catalysis* 168 (1997) 110–116.

[37] A.M. Venezia, R. Murania, G. Pantaleo, G. Deganello, *Journal of Catalysis* 251 (2007) 94–102.

[38] S.M. Kanan, N. Abdo, M. Khalil, X. Li, I.A. Abu-Yousef, F. Barilrobert, H.H. Patterson, *Applied Catalysis B* 106 (2011) 350–358.

[39] G. Busca, T. Montanari, M. Bevilacqua, E. Finocchio, *Colloids and Surfaces A: Physicochemical and Engineering Aspects* 320 (2008) 205–212.

[40] J. Yarwood, *Spectroscopy and Structure of Molecular Complexes*, Plenum, London, 1973, p. 141.

[41] K.F. Purcell, R.S. Drago, *Journal of the American Chemical Society* 88 (1966) 919–924.

[42] B.N. Storhoff, H.C. Lewis Jr., *Coordination Chemistry Reviews* 23 (1977) 1–29.

[43] W.J. Bland, P.D.W. Kemmitt, R.D. Moore, *Journal of the Chemical Society, Dalton Transactions* 12 (1973) 1292–1295.

[44] J. Raskó, J. Kiss, *Applied Catalysis A* 303 (2006) 56–61.

[45] J.W. London, A.T. Bell, *Journal of Catalysis* 31 (1973) 96–109.

[46] R. Zhang, W.Y. Teoh, R. Amal, B. Chen, S. Kaliaguine, *Journal of Catalysis* 272 (2010) 210–219.

[47] J. Raskó, J. Kiss, *Applied Catalysis A* 298 (2006) 115–126.

[48] T. Nanba, S. Masukawa, J. Uchisawa, A. Obuchi, *Journal of Catalysis* 259 (2008) 250–259.

[49] E. Kukulska-Zajac, K. Góra-Marek, J. Datka, *Microporous and Mesoporous Materials* 96 (2006) 216–221.

[50] P. Davit, G. Martra, S. Coluccia, V. Augugliaro, E.G. López, V. Loddo, G. Marcì, L. Palmisano, M. Schiavello, *Journal of Molecular Catalysis A: Chemical* 204–205 (2003) 693–701.

[51] K. Góra-Marek, B. Gil, M. Sliwa, J. Datka, *Applied Catalysis A* 330 (2007) 33–42.

[52] B.H. Chen, N. Liu, X.Y. Liu, R.D. Zhang, Y.P. Li, Y.X. Li, X.L. Sun, *Catalysis Today* 175 (2011) 245–255.

[53] J.D.F. Marsh, W.B.S. Newling, J. Rich, *Journal of Applied Chemistry* 2 (1952) 681–684.